

Electronic Supplementary Information

Fe₃O₄@Au@mSiO₂ as Enhancing Nanoplatform for Rose Bengal Photodynamic Activity

I. Rosa-Pardo,^a M. Roig-Pons,^a A. A. Heredia,^a † J. V. Usagre,^a A. Ribera,^a
R. E. Galian^{a*} and J. Pérez-Prieto^{a*}

Figure S1: (a) UV-visible spectra of Fe ₃ O ₄ nanoparticles dispersed in toluene; inset: picture of the dispersion; b) and c) HRTEM images of Fe ₃ O ₄ nanoparticles (5.1 ± 0.9 nm), scale bar 2 nm (b) and 20 nm (c).	S2
Table S1: Top: HRTEM images showing the evolution of the Au shell growth on the Fe ₃ O ₄ seeds. Bottom: UV-Vis absorption spectra of the resulting NPs.	S3
Figure S2: EDX spectrum of Fe ₃ O ₄ @Au-3 core-shell NPs.	S4
Figure S3: PXRD spectrum of Fe ₃ O ₄ @Au-3 core-shell NPs.	S4
Figure S4: TGA thermogram and first derivative curves of Fe ₃ O ₄ and Fe ₃ O ₄ @Au-3 core-shell NPs.	S5
Figure S5: TGA thermogram and first derivative curves of oleylamine and oleic acid.	S6
Figure S6: Temperature dependence of the measured magnetic susceptibility of Fe ₃ O ₄ (blue) and Fe ₃ O ₄ @Au NPs (red).	S7
Figure S7: Top: magnetization versus the magnetic field at 5 K of Fe ₃ O ₄ (blue) and Fe ₃ O ₄ @Au NPs (red). Bottom: zoom of the graph magnetisation versus the magnetic field for both samples.	S8
Figure S8: Absorption spectrum of Fe ₃ O ₄ @Au-3 NPs capped with CTAB and dispersed in water.	S9
Figure S9: TEM, SEM and HRTEM images of mSiO ₂ (97 ± 6 nm) synthesised under optimal conditions; scale bar of a) 200 nm, b) 400 nm, c) 50 nm and d) 20 nm.	S10
Figure S10: (left) TEM images of Au@mSiO ₂ (66 ± 6 nm) and (right) Fe ₃ O ₄ @mSiO ₂ (50 ± 5 nm); scale bar of 50 nm.	S11
Figure S11: Absorption and emission spectra of (a, b) RB, (c, d) mSiO ₂ -RB, (e, f) Fe ₃ O ₄ @mSiO ₂ -RB, and (g, h) Fe ₃ O ₄ @Au@mSiO ₂ -RB in water.	S12
Figure S12: Comparison between the FTIR spectra of RB, Fe ₃ O ₄ @Au@mSiO ₂ -RB, and mSiO ₂ -NH ₂ , thus demonstrating the important changes of the RB signals when the photosensitizer is anchored to the silica pores.	S13
Figure S13: Top: scheme of the reaction of the probe (ADBA) with singlet oxygen. Bottom: (left) UV-vis spectra of the water solution of RB (1.6 μM) and ADBA (20 μM) irradiated with visible light to up to 20 minutes; (right) Ln (A ₀ /A) of ADBA at 380 nm vs. irradiation time.	S14
Figure S14: (Left) Absorption spectra of a water dispersion of Fe ₃ O ₄ @Au@mSiO ₂ -RB and ADBA irradiated with visible light to up to 20 minutes. (Right) Ln (A ₀ /A) of ADBA at 380 nm vs. irradiation time..	S14
Table S2: Optimization parameters for the nanoplatform synthesis.	S15
Figure S15: Absorption spectrum of an acetonitrile dispersion of Fe ₃ O ₄ @Au@mSiO ₂ -RB and Rose Bengal.	S16
Figure S16: Transient absorption spectra of RB and Fe ₃ O ₄ @Au@mSiO ₂ -RB recorded 5 μs after the laser pulse (532 nm) in acetonitrile under nitrogen atmosphere.	S16
Figure S17: Kinetic trace recorded at 610 nm after excitation (532 nm) of Fe ₃ O ₄ @Au@mSiO ₂ -RB and RB in acetonitrile under nitrogen atmosphere.	S17

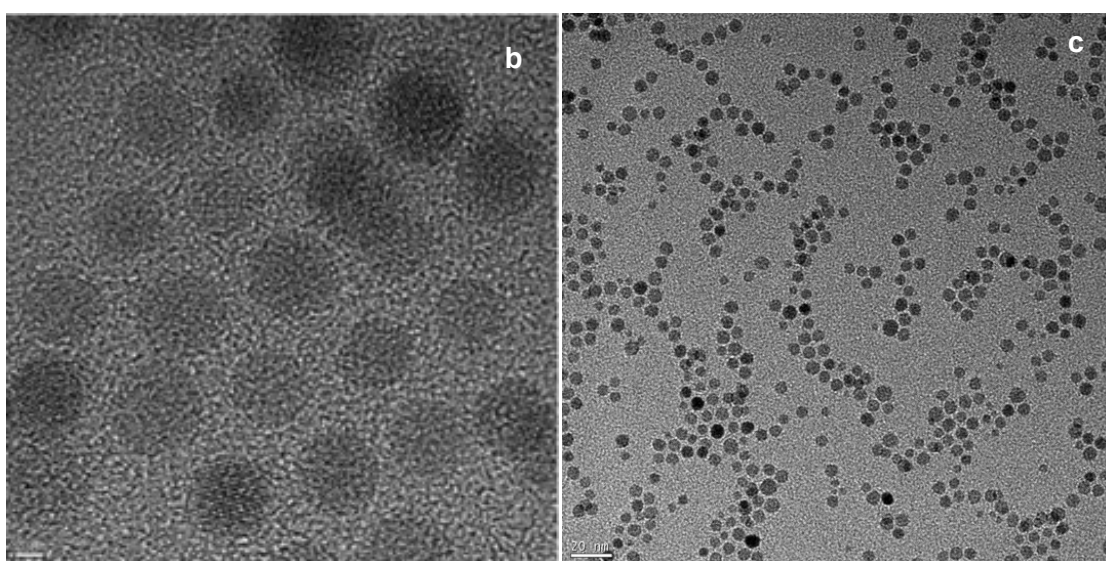
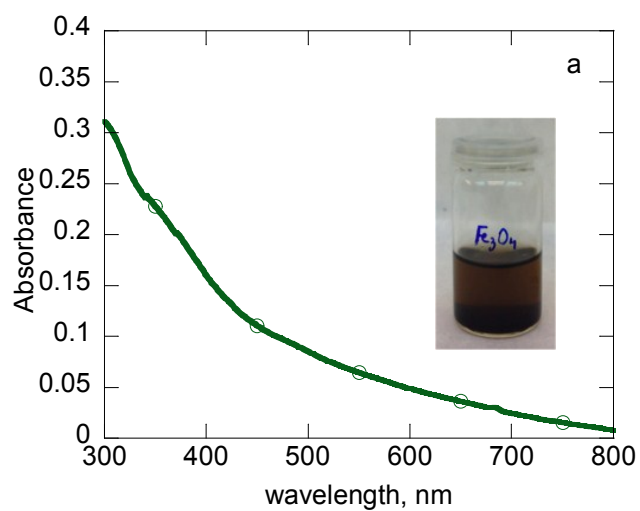
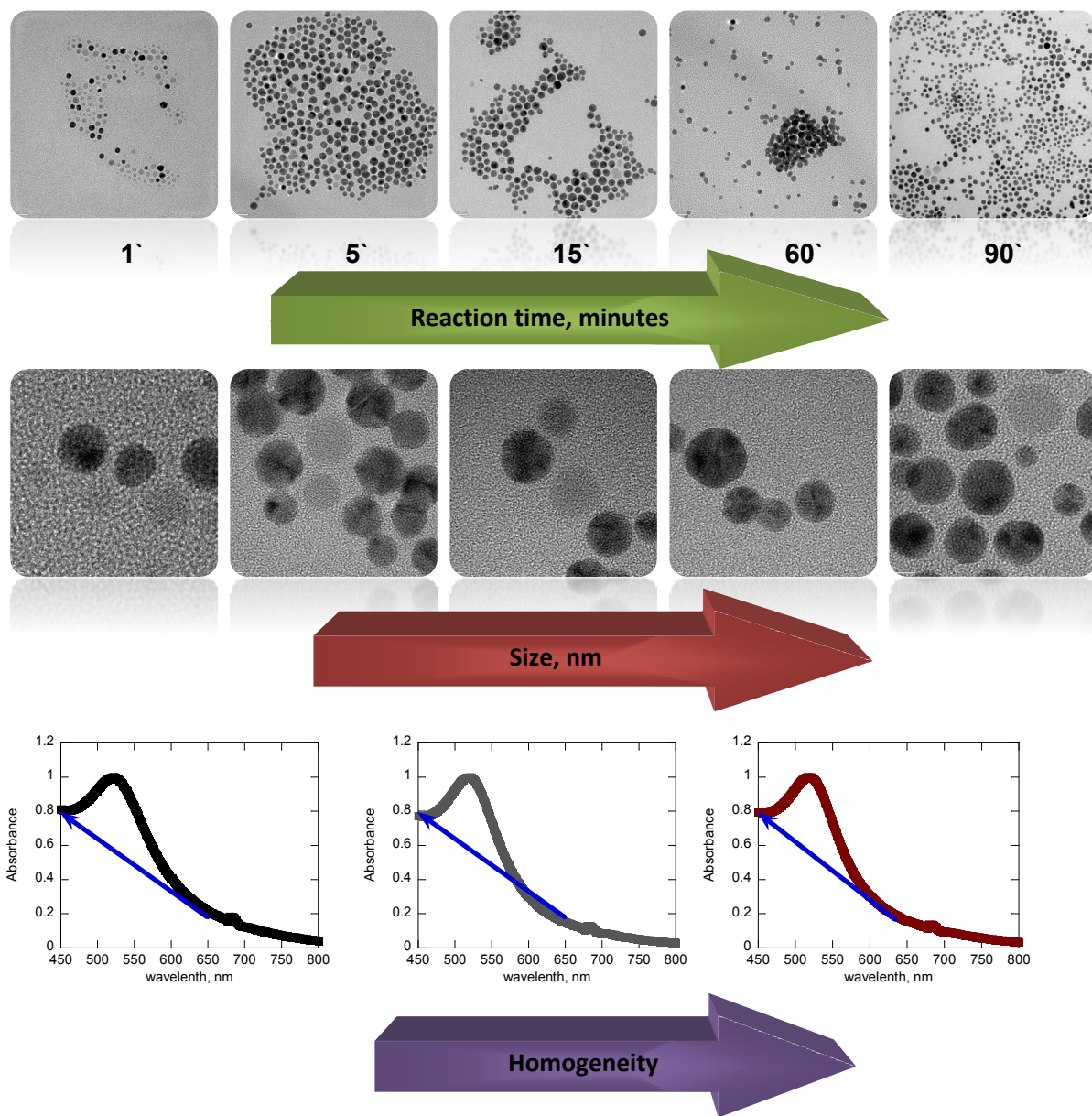


Figure S1: (a) UV-visible spectra of Fe₃O₄ nanoparticles dispersed in toluene; inset: picture of the dispersion; b) and c) HRTEM images of Fe₃O₄ nanoparticles (5.1 ± 0.9 nm), scale bar 2 nm (b) and 20 nm (c).

Table S1: (Top) HRTEM images showing the evolution of the Au shell growth on the Fe_3O_4 seeds. (Bottom) UV-Vis absorption spectra of the resulting NPs.



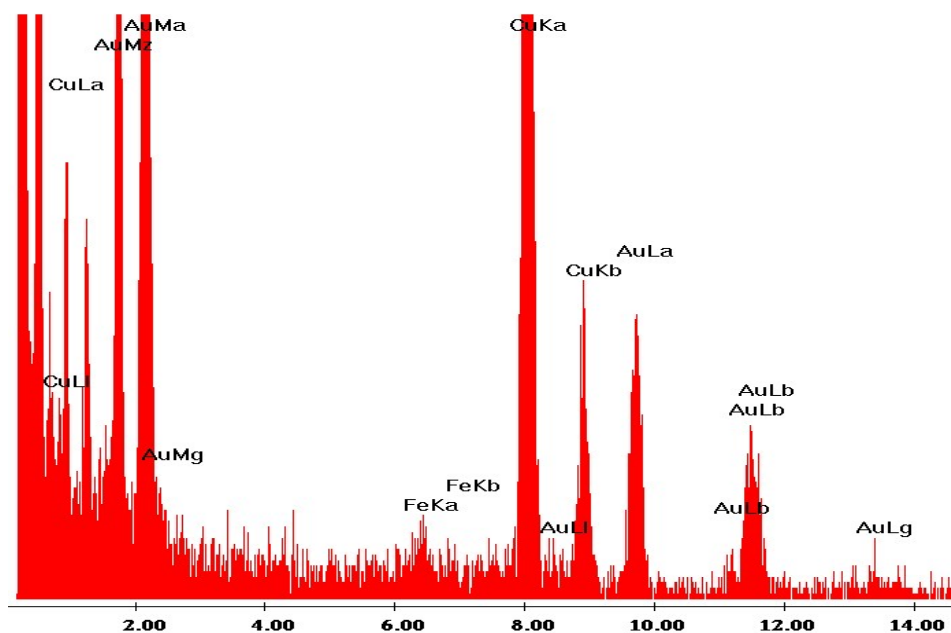


Figure S2: EDX spectrum of Fe₃O₄@Au-3 core-shell.

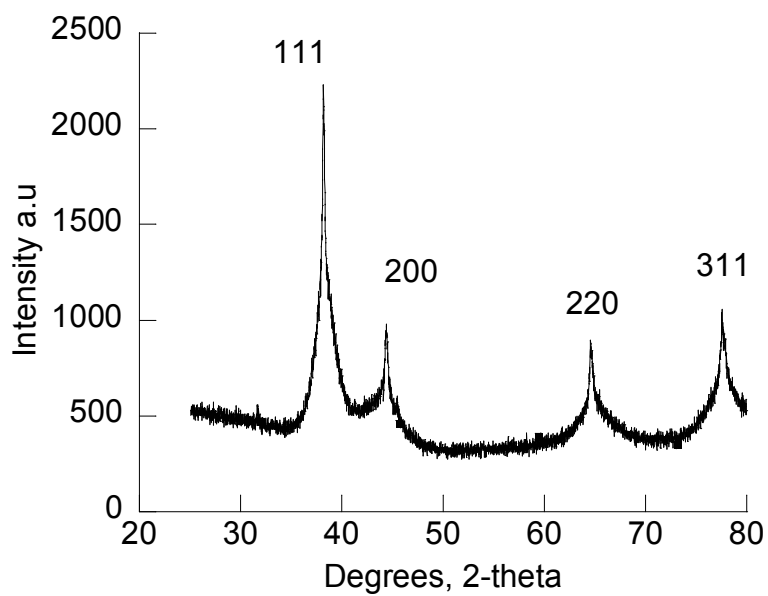


Figure S3: PXRD spectrum of Fe₃O₄@Au-3 core-shell NPs.

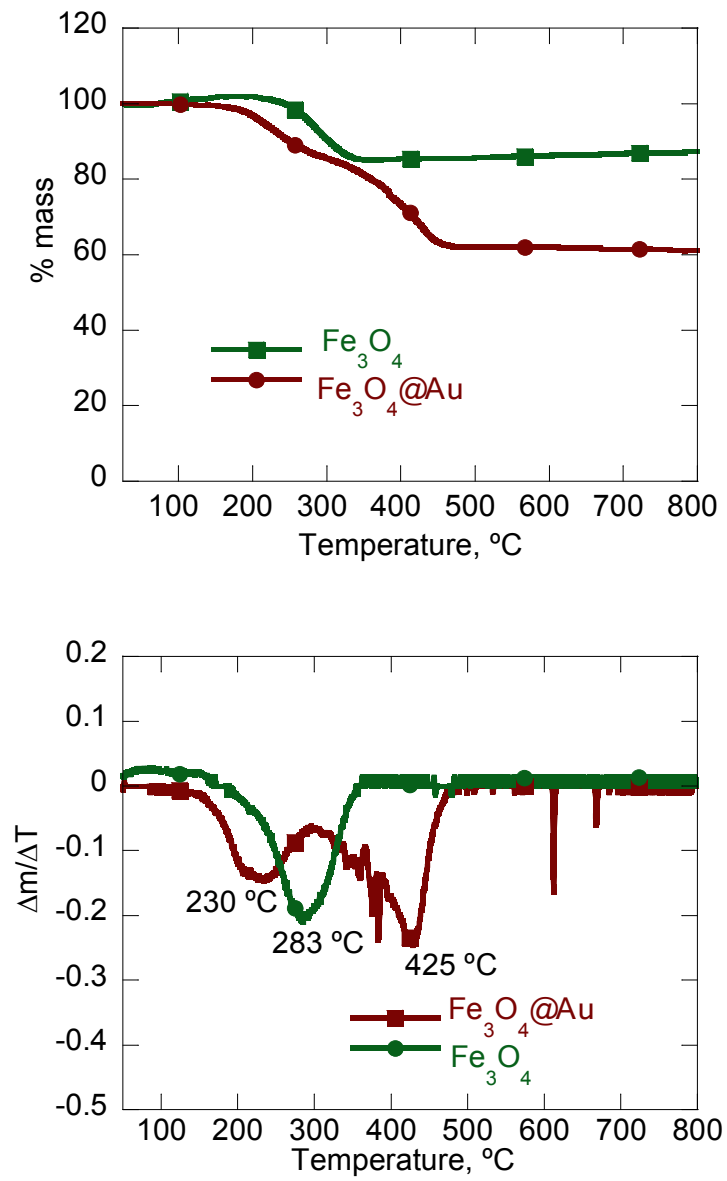


Figure S4: TGA thermogram and first derivative curves of Fe₃O₄ and Fe₃O₄@Au-3 core-shell NPs.

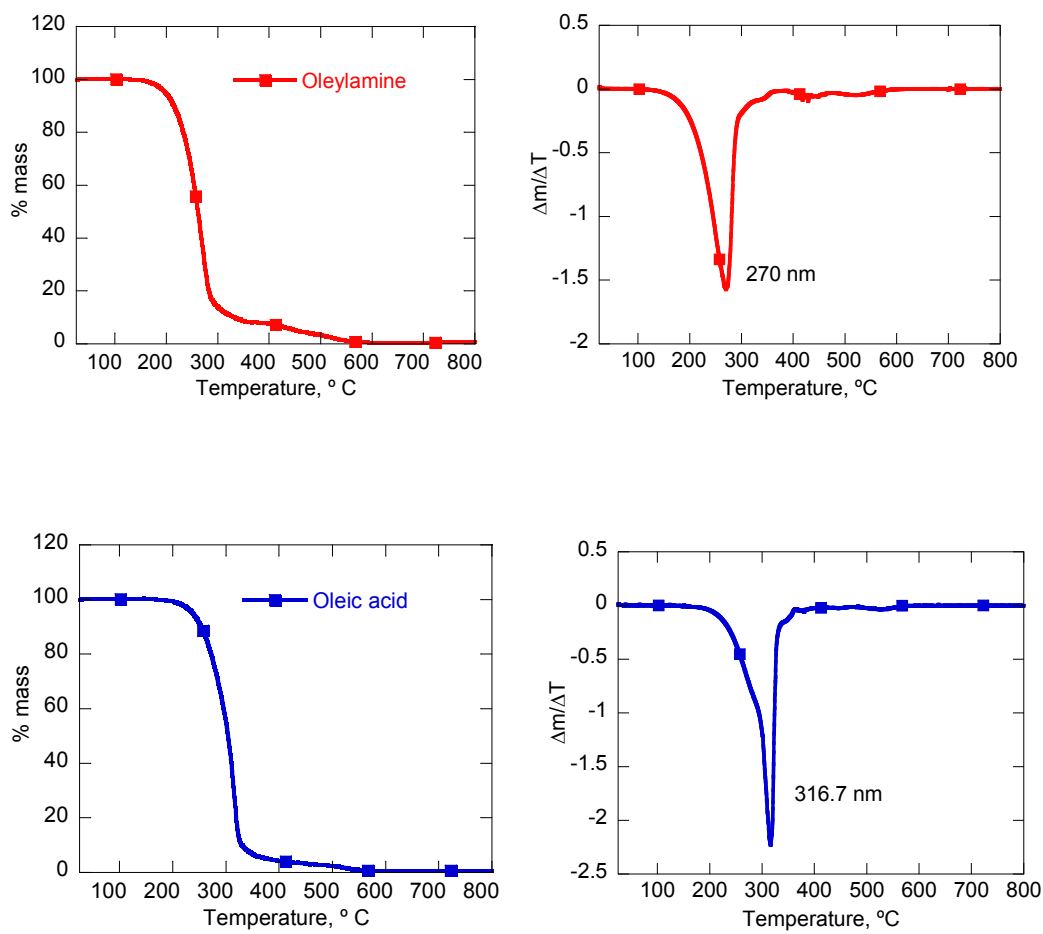


Figure S5: TGA thermogram and first derivative curves of oleylamine and oleic acid.

Magnetic Properties of the Fe₃O₄@Au NPs

The saturation magnetization, coercivity, susceptibility and blocking temperature of the core-shell Fe₃O₄@Au NPs were determined from SQUID measurements and compared with those of Fe₃O₄. In Figure S3 the temperature dependence of the measured magnetic susceptibility for Fe₃O₄ and Fe₃O₄@Au NPs is reported. Powdered samples were initially cooled in a zero field to 2 K, then a field of 10 Oe was applied, and the magnetization was recorded while the temperature was increased as a zero-field-cool (zfc) curve. As soon as the temperature arrives to 300 K, the samples were cooled and the magnetization was registered as a field-cool (fc) curve. The zfc curves present a maximum susceptibility at 40 K corresponding to a value of 0.125 emu·Oe⁻¹·g⁻¹(Fe₃O₄) for the uncoated magnetite and a value of 0.003 emu·Oe⁻¹·g⁻¹(Fe₃O₄) at 26 K for the core-shell sample. Taking in to account the data for the samples were corrected, by considering the fraction of Fe₃O₄ obtained from both thermal gravimetric analysis and ICP-OES analysis, it is clear that the magnetic susceptibility is much smaller for the core-shell sample in comparison with the uncoated sample. On the other hand, the temperature for the maximum of the susceptibility is indicative of the blocking temperature being in the case of the uncoated sample higher (40 K) that the core-shell sample (26 K). The fact that the temperature blocking decreases is a reflect the diminution coupling of the magnetic moments as a result of the increased interparticle spacing of magnetic cores,¹ consequence to the presence of the gold shell in the case of Fe₃O₄@Au NPs in addition to the organic capping that is present in both cases.

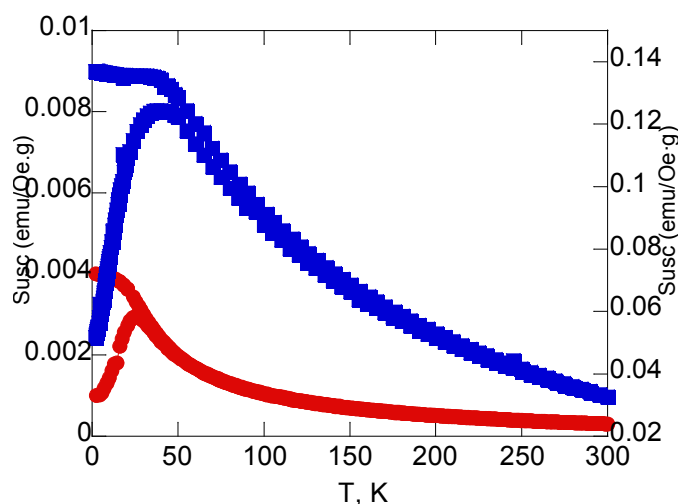


Figure S6: Temperature dependence of the measured magnetic susceptibility of Fe₃O₄ (blue) and Fe₃O₄@Au NPs (red).

¹ A.K. Boal; B.L. Frankamp; O. Uzun; M. Tuominen, V.M. Rotello. Chem. Mater., 2004, 16, 3252.

In Figure S7, the magnetization versus the magnetic field at 5 K by cycling the field between – 50 KOe to 50 KOe is reported for both samples. Clearly, the magnitude of the magnetization for uncoated sample ($110 \text{ emu}\cdot\text{g}^{-1}(\text{Fe}_3\text{O}_4)$) is much bigger than that of the core-shell sample ($3 \text{ emu}\cdot\text{g}^{-1}(\text{Fe}_3\text{O}_4)$). The mass of Fe_3O_4 was calculated from the weight of the respective sample, considering the TGA data and the results of the ICP-OES analysis. In addition, the core-shell sample do not presents saturation magnetization in the magnetic field range even at 50 KOe. Finally, an important difference is observed between the coated and uncoated samples. Coercivities measured at 5 K presented 70 and 240 Oe for Fe_3O_4 and $\text{Fe}_3\text{O}_4@Au$ Nanoparticles, respectively. The increased coercivity for the coated sample could be associated with the larger particle size, that provoke a less-effective coupling of the magnetic dipole moments, in the same way as concluded from the magnetic susceptibility measures. In the opposite, the Fe_3O_4 sample presents nanoparticles that are coupled more effectively producing a lower coercivity.

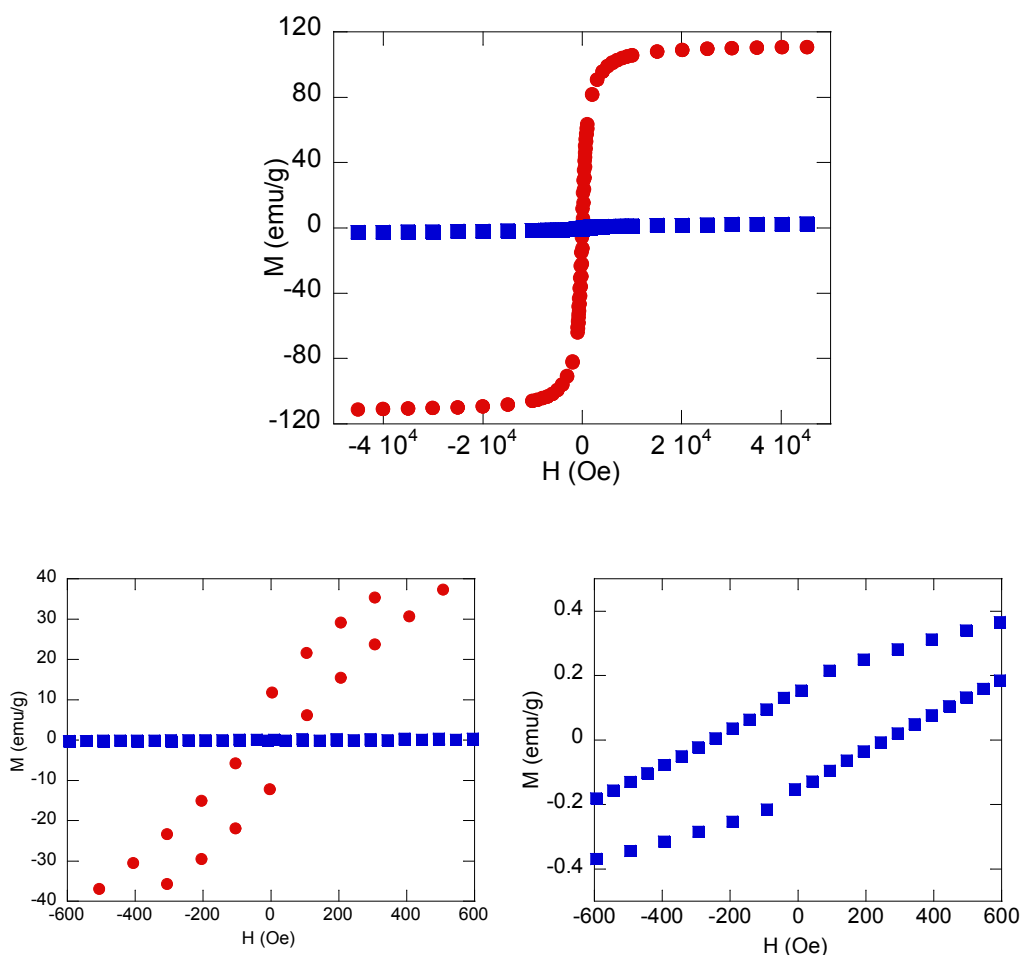


Figure S7: Top: magnetization versus the magnetic field at 5 K of Fe_3O_4 (blue) and $\text{Fe}_3\text{O}_4@Au$ NPs (red). Bottom: zoom of the graph magnetization versus the magnetic field for both samples.

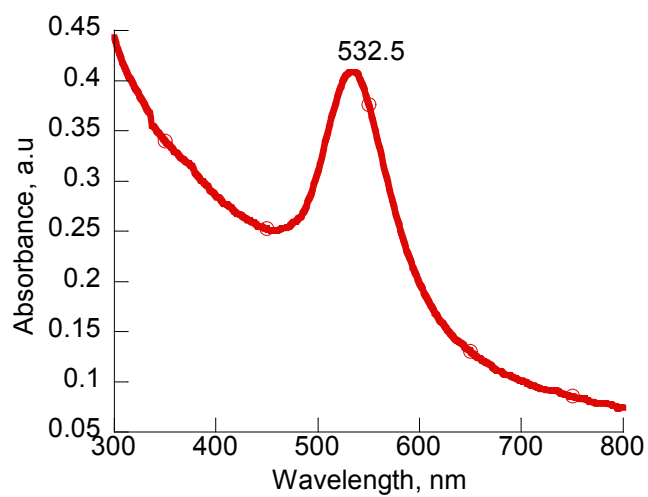


Figure S8: Absorption spectrum of Fe_3O_4 @Au-3 NPs capped with CTAB and dispersed in water.

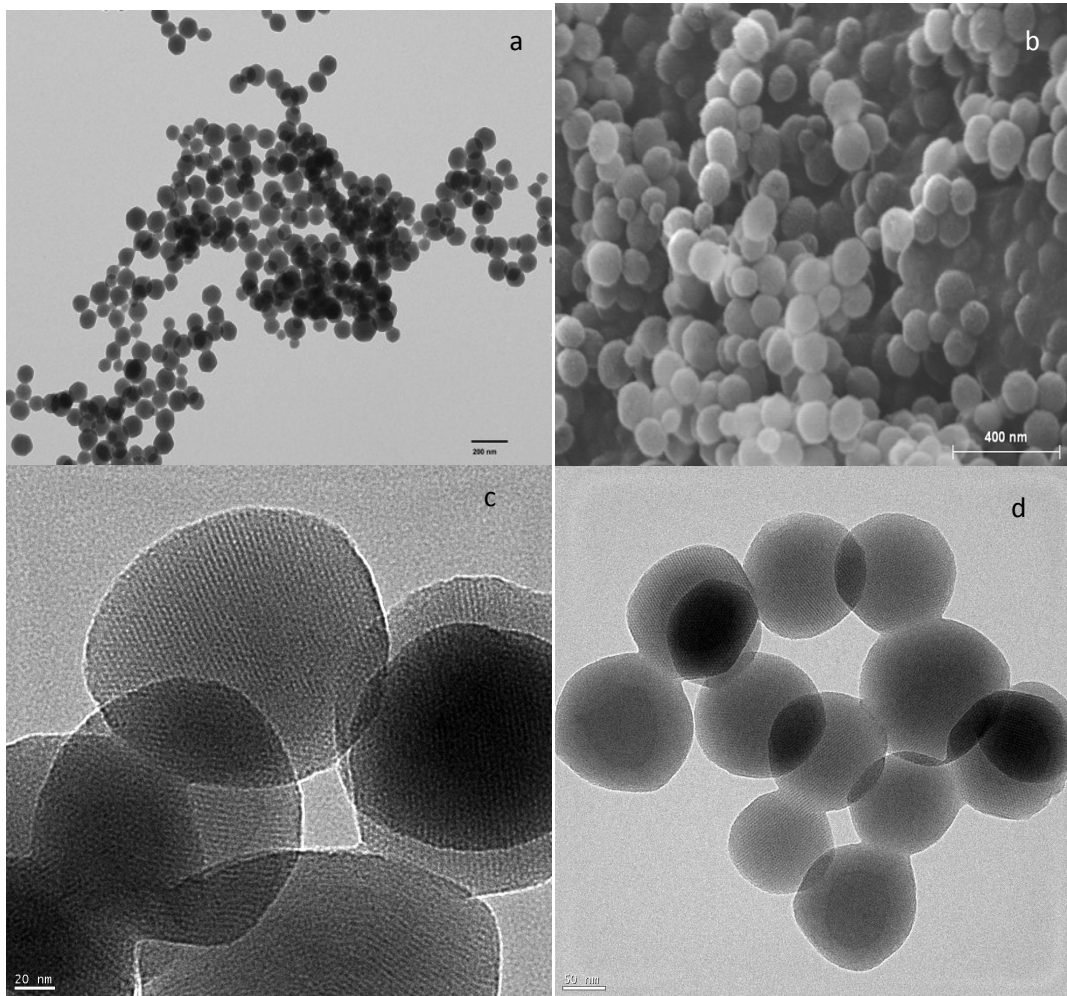


Figure S9: TEM, SEM and HRTEM images of mSiO₂ (97 ± 6 nm) synthesised under optimal conditions; scale bar of a) 200 nm, b) 400 nm, c) 50 nm and d) 20 nm.

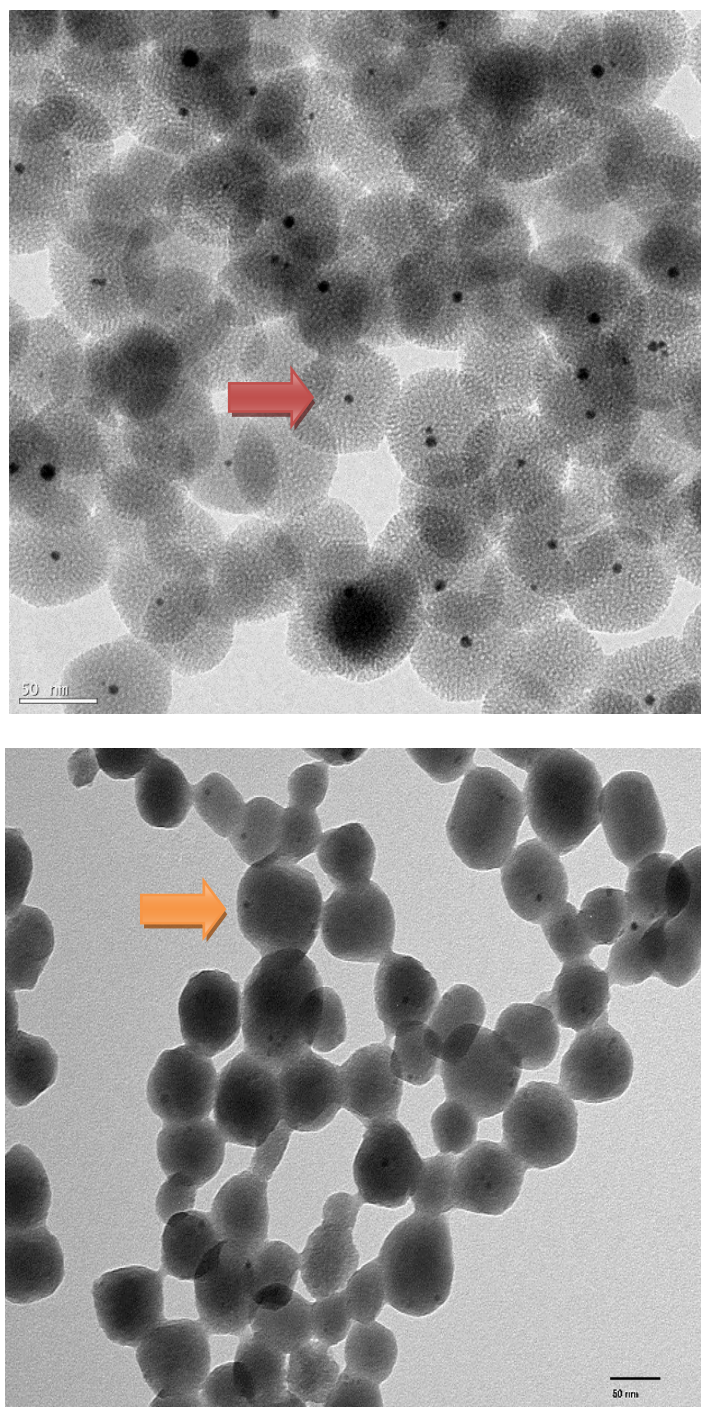
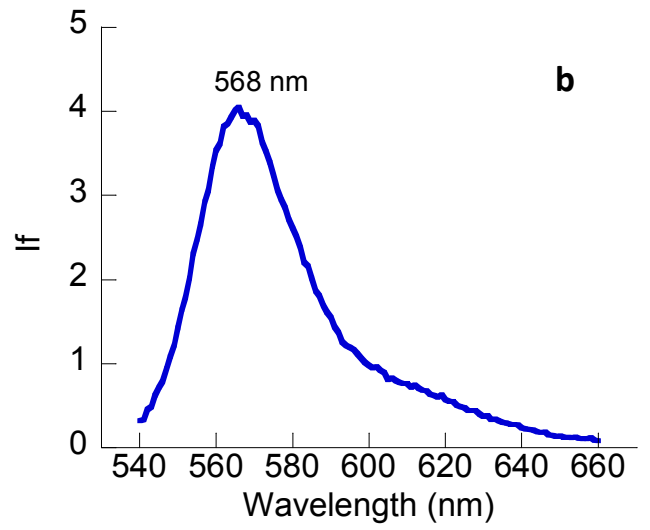
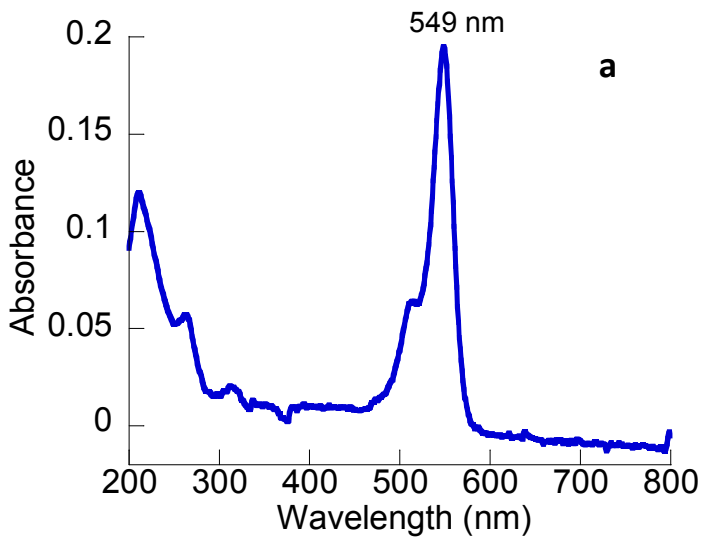


Figure S10: (left) TEM images of Au@mSiO₂ (66 ± 6 nm) and (right) Fe₃O₄@mSiO₂ (50 ± 5 nm) NPs; scale bar of 50 nm.

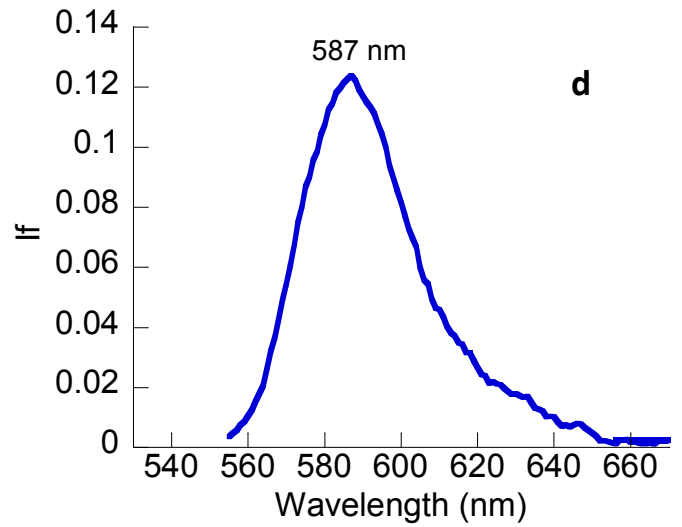
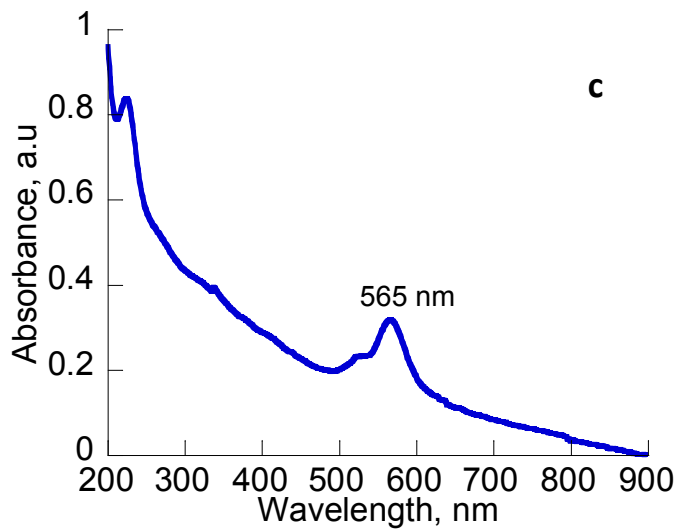
Absorption spectra

Emission spectra (λ exc. = 520 nm)

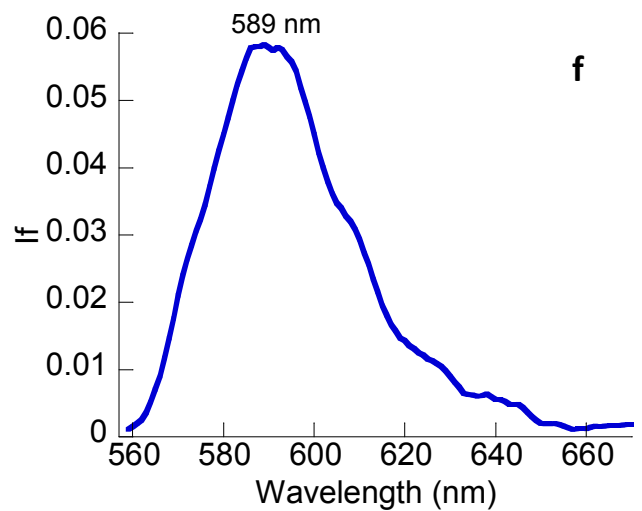
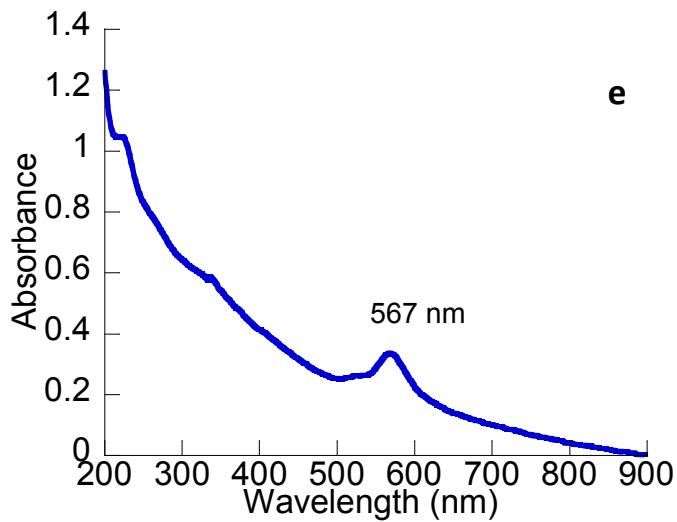
RB



mSiO₂-RB



Fe₃O₄@mSiO₂-RB



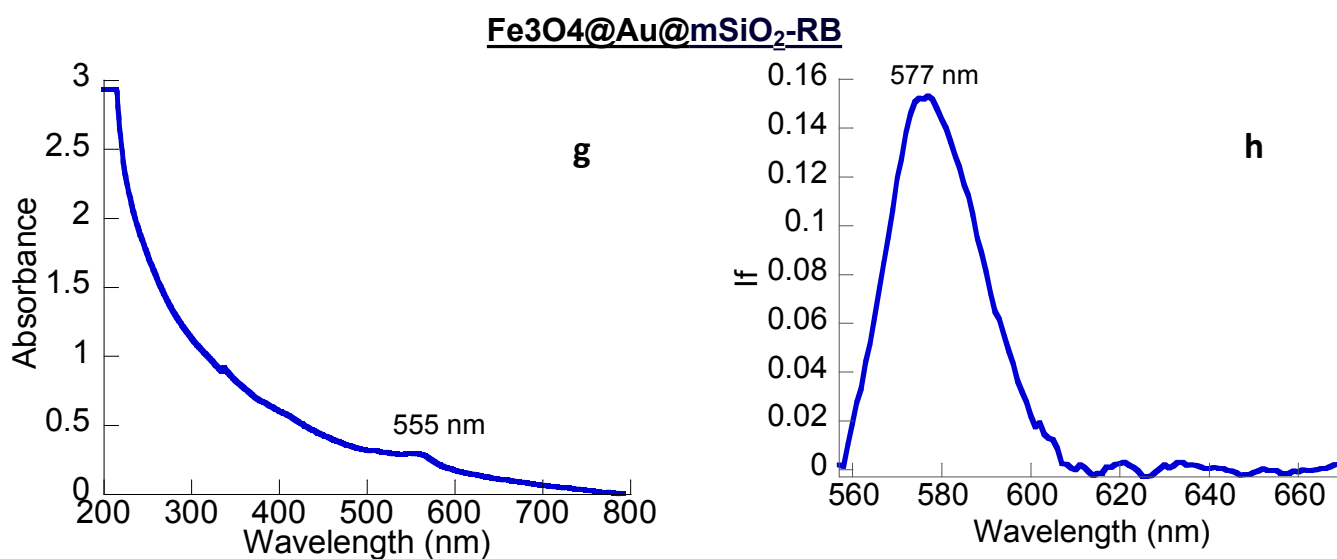


Figure S11: Absorption spectra in water of (a) RB, (c) mSiO₂-RB, (e) Fe₃O₄@mSiO₂-RB, and (g) Fe₃O₄@Au@mSiO₂-RB. Emission spectra obtained by subtracting the scattering: (b) RB, (d) mSiO₂-RB, (f) Fe₃O₄@mSiO₂-RB, and (h) Fe₃O₄@Au@mSiO₂-RB.

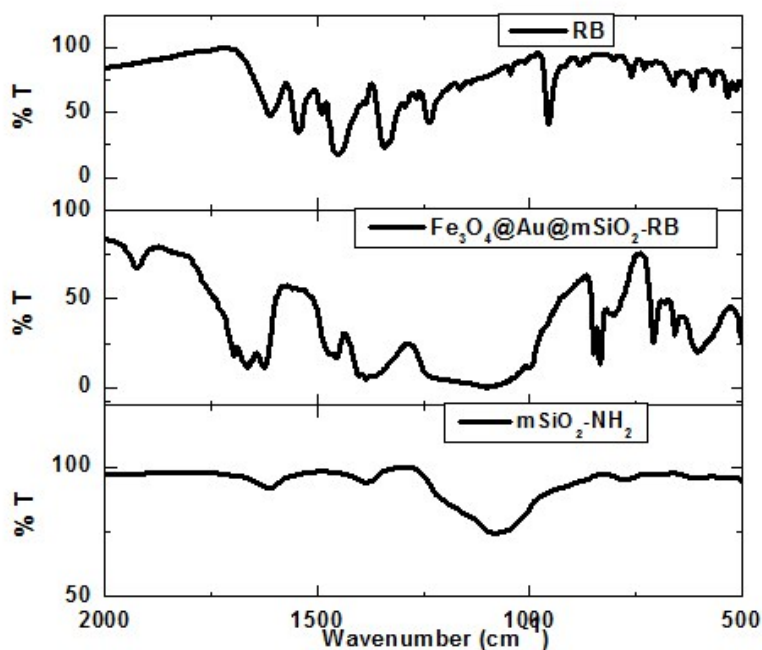


Figure S12: Comparison between the FTIR spectra of RB, Fe₃O₄@Au@mSiO₂-RB, and m-SiO₂-NH₂, thus demonstrating the important changes of the RB signals when the photosensitizer is anchored to the silica pores.

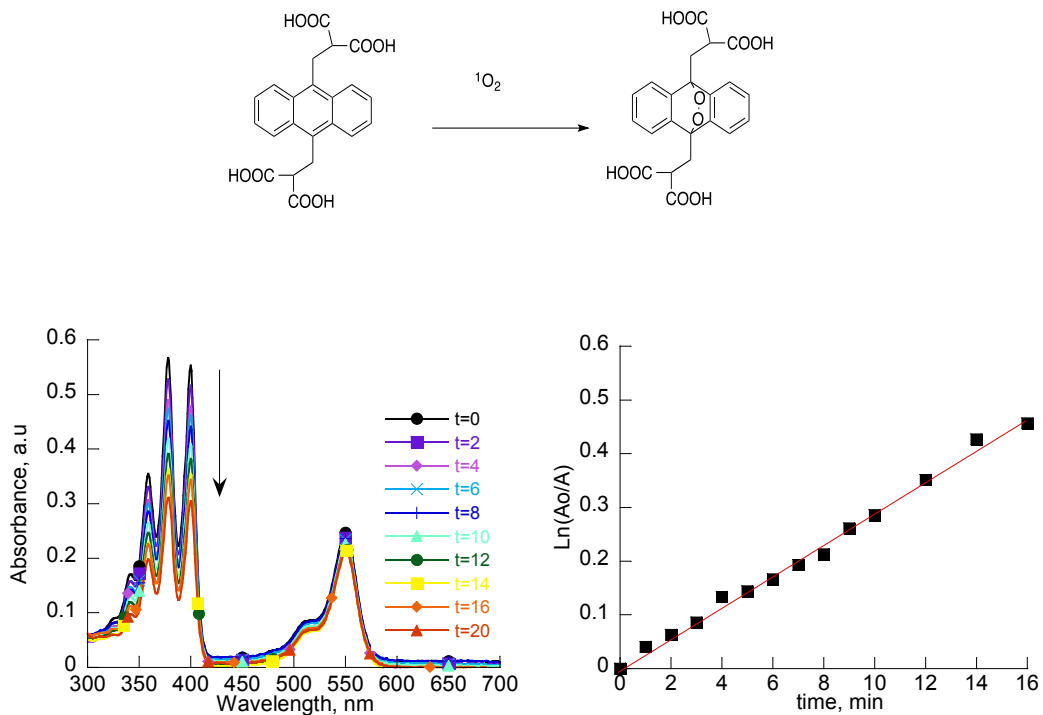


Figure S13: Top: scheme of the reaction of the probe (ADBA) with singlet oxygen. Bottom: (left) UV-vis spectra of the water solution of RB (1.6 μM) and ADBA (20 μM) irradiated with visible light to up to 20 minutes; (right) $\text{Ln}(A_0/A)$ of ABDA at 380 nm vs. irradiation time.

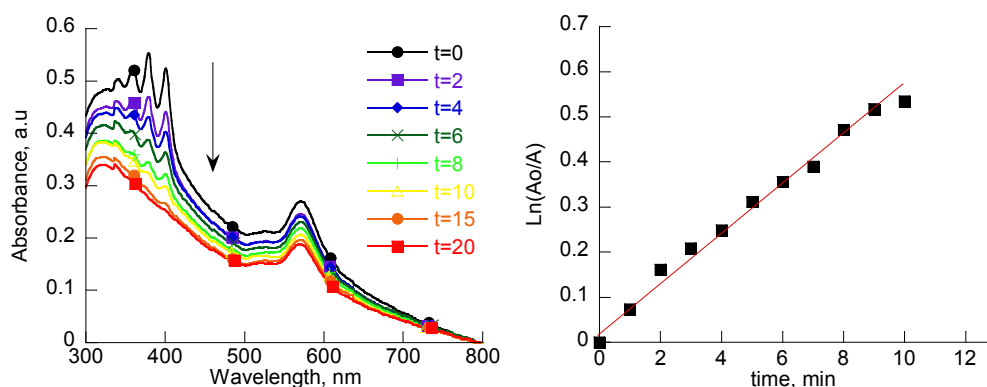


Figure S14: (Left) Absorption spectra of a water dispersion of $\text{Fe}_3\text{O}_4@Au@m\text{SiO}_2\text{-RB}$ and ABDA irradiated with visible light to up to 20 minutes. (Right) $\text{Ln}(A_0/A)$ of ABDA at 380 nm vs. irradiation time.

Table S2: Optimization parameters for the nanoplatform synthesis.

#	NPs Fe ₃ O ₄ @Au (mg)	μL CTAB 55 mM	Reaction time
1	0.22	482 μL	60 '
2	0.264	478 μL	60 '
3	0.33	473 μL	60 '
4	0.374	469 μL	60 '
5	0.44	464 μL	60 '
6	0.44	464 μL	30 '
7	0.44	464 μL	90 '
8	0.484	460 μL	60 '
9	0.88	425 μL	60 '

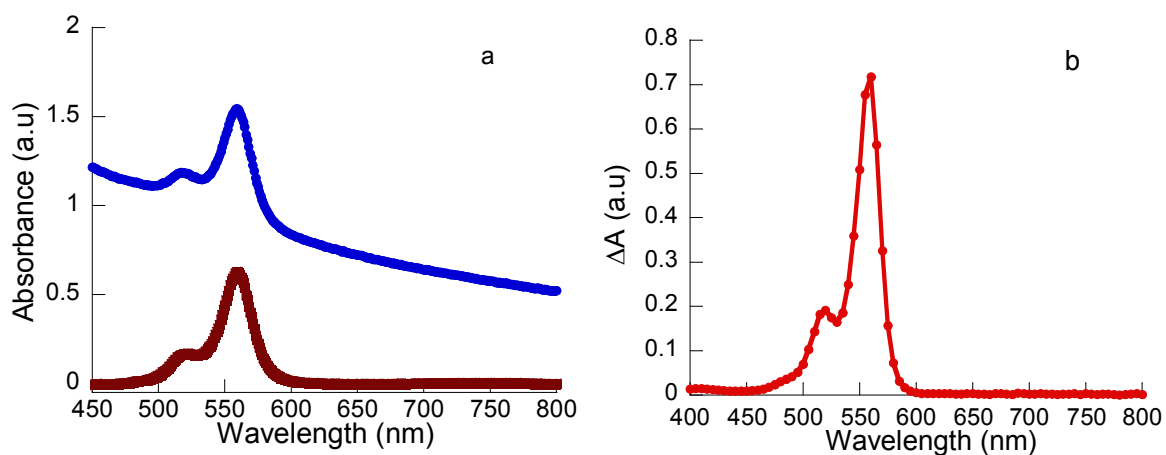


Figure S15: a) Absorption spectrum of an acetonitrile dispersion of $\text{Fe}_3\text{O}_4@Au@m\text{SiO}_2\text{-RB}$ used for the laser experiments (blue); the spectrum after subtraction of the scattering contribution is shown in dark red; b) Absorption spectrum of an acetonitrile solution of Rose Bengal in acetonitrile.

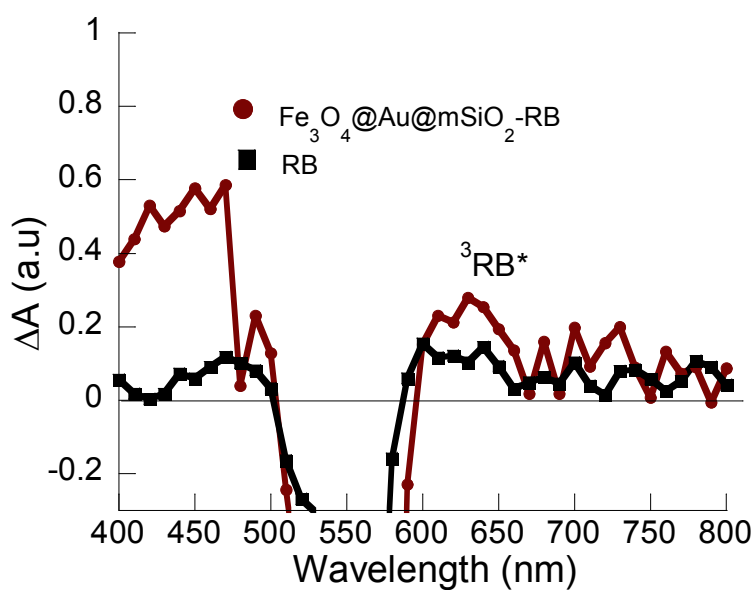


Figure S16: Transient absorption spectra of RB (black) and $\text{Fe}_3\text{O}_4@Au@m\text{SiO}_2\text{-RB}$ (dark red) recorded 5 μs after the laser pulse (532 nm) in acetonitrile under nitrogen atmosphere.

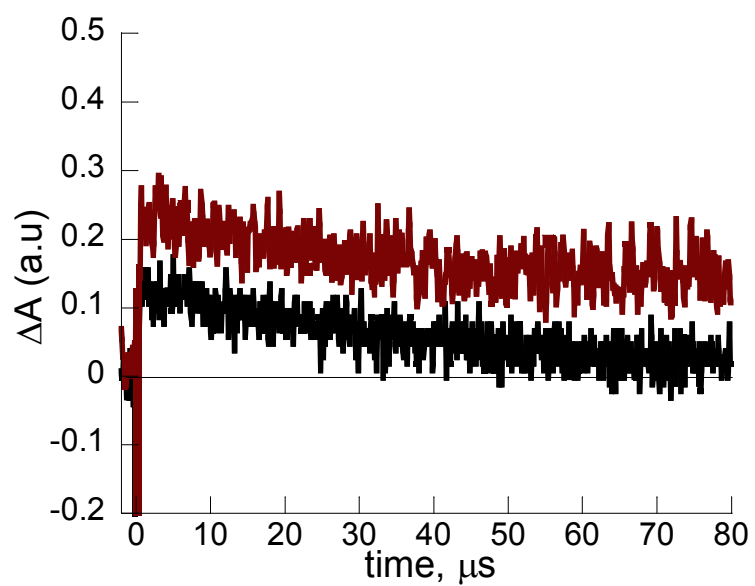


Figure S17: Kinetic trace at 610 nm recorded after excitation (532 nm) of $\text{Fe}_3\text{O}_4@Au@m\text{SiO}_2\text{-RB}$ (dark red) and RB (black) in acetonitrile under nitrogen atmosphere.